Diphenyleneiodonium chloride inhibits MYCN-amplified neuroblastoma by targeting MYCN induced mitochondrial alterations

Authors

Soraya Epp[1,9], Stephanie Maher[1,9], Amirah Adlina Abdul Aziz[1], Simone Marcone[1], Donagh Egan[1], Saija Haapa-Paananen[2,6], Vidal Fey[2,7], Kristiina Iljin[2,8], Kieran Wynne[1,3], Lasse D. Jensen[4,5], *Walter Kolch[1,3,10], *Melinda Halasz[1,3,10]

[1] Systems Biology Ireland, School of Medicine, University College Dublin, Dublin, Ireland
[2] VTT Technical Research Center of Finland, Turku, Finland
[3] Conway Institute of Biomolecular and Biomedical Research, University College Dublin, Ireland
[4] Department of Health, Medicine and Care, Division of Diagnostics and Specialist Medicine, Linköping University, Linköping, Sweden
[5] BioReperia AB, Linköping, Sweden
[6] Present address: FINBB - Finnish Biobank Cooperative, Turku, Finland
[7] Present address: Faculty of Medicine and Health Technology, Tampere University, Tampere, Finland
[8] Present address: VTT Technical Research Centre of Finland Ltd., Espoo, Finland
[9] These authors contributed equally
[10] Senior authors

*Correspondence: melinda.halasz@ucd.ie, walter.kolch@ucd.ie

Abstract

High-risk neuroblastoma is one of the most lethal childhood cancers. Half of these tumors are driven by MYCN gene amplification (MNA). Despite intensive chemo- and radiotherapy, only 40% of patients survive, and they often suffer from severe long-term side effects of these genotoxic treatments. Thus, new therapies are needed that are less toxic and more efficacious. Here, we identified diphenyleneiodonium (DPI) as a tool compound that preferentially targets MNA neuroblastoma. Using proteomic assays we investigated the DPI mode of action, finding that DPI induces the proteasomal degradation of MYCN and could reverse some alterations induced by high levels of MYCN. These include profound changes in the expression of proteins participating in the mitochondrial electron transport chain. Metabolic and biological assays suggested that alterations in mitochondrial function and the associated production of reactive oxygen species (ROS) are critical DPI targets in the context of MNA. DPI reduced the survival, and malignant transformation of neuroblastoma across a panel of cell lines at clinically achievable concentrations. DPI also shrank tumors and prevented metastatic spread in zebrafish models of MYCN-driven neuroblastoma. These findings suggest that processes impacted by complex I inhibitors could be valuable new targets for the development of non-genotoxic drugs against high-risk MNA neuroblastoma.

Keywords

Neuroblastoma, MYCN, mitochondria

Graphical abstract

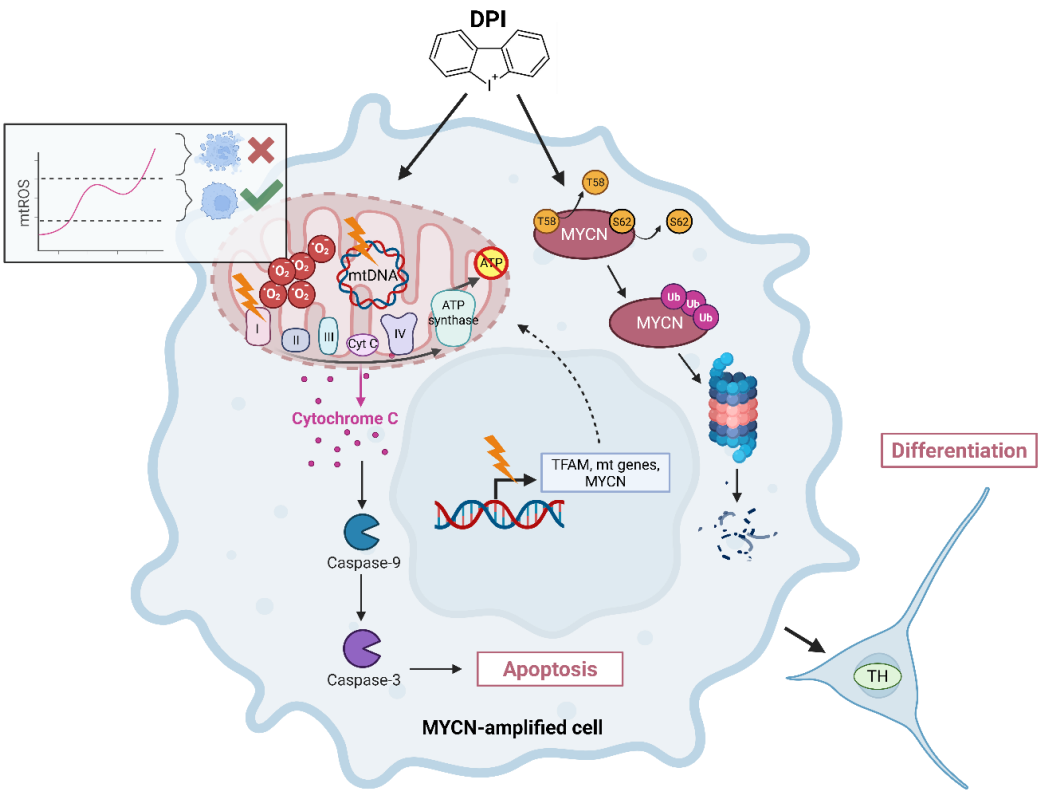

Introduction

Neuroblastoma (NB) is a tumor of the peripheral sympathetic nervous system that accounts for only 6% of childhood cancer cases, but for 15% of deaths from childhood cancers[1]. This disproportionate risk is mainly due to high-risk NB that is driven by amplification of the MYCN gene. Patients with MYCN amplified (MNA) disease represent ca. 20% of all patients, and their 5-year event-free survival is only around 40%. They are usually treated with a combination of intensive genotoxic chemotherapy and radiation therapy. Nevertheless, many patients relapse, leaving them with limited or no treatment options. Furthermore, survivors may have severe long-term toxicities, including cardiovascular problems, hearing loss, secondary cancers, infertility, and endocrine deficiencies[2]. Thus, the current challenge is to identify therapies that are not genotoxic and more efficacious. This means that we must expand the drug target space and find compounds with new modes of action.

The obvious target is MYCN. It is a transcription factor with pleiotropic functions and considered as a master regulator of NB development[3]. However, MYCN is difficult to target directly as it lacks apparent pockets where drugs can bind to[4]. Thus, the current main strategies are to block critical MYCN functions and mechanisms that stabilize the inherently unstable MYN protein[5, 6]. However, so far none of these strategies have produced a clinically applicable approach.

Here, we used NB cell lines with regulatable MYCN expression to screen for compounds that preferentially inhibit cells with high MYCN levels. Amongst the most selective compounds targeting high MYCN expressing cells was diphenyleneiodonium chloride (DPI). This compound was originally described as NADPH oxidase inhibitor that reduces the generation of reactive oxygen species (ROS) in the mitochondria, but also has a broader range of targets including NAD/NADP-dependent enzymes in the tricarboxylic acid cycle and pentose phosphate pathway[7]. Newer studies showed that DPI also can induce ROS production by enhancing superoxide production from forward electron transport in complex I of the electron transport chain (ETC)[8]. Malignant cells, including NB cells, often produce more ROS than normal cells, as their increased demand for energy enhances oxidative phosphorylation (OXPHOS) and accompanying ROS production. This mechanism has been identified as a targetable vulnerability of MNA cells[9, 10]. Interestingly, MNA NB cells feature an enrichment of the ROS induced COSMIC mutational signature 18[11], suggesting that ROS contribute to the pathogenetic mechanism of NB.

Investigating the DPI mode of action in MNA cells, we found that DPI targets alterations in mitochondrial metabolism including OXPHOS and ROS production. Assessing DPI in both *in vitro* and in MYCN-driven zebrafish models of NB showed that DPI could efficiently counteract NB growth.

Results

DPI decreases viability more effectively in MNA cells and drives widespread proteomic alterations, particularly in mitochondrial functions

In order to screen for compounds that preferentially interfere with the viability of MYCN overexpressing NB, we used the SH-SY5Y cell line harboring a doxycycline inducible MYCN transgene (SY5Y/6TR (EU)/pTrex-Dest-30/MYCN cells; called SH-SY5Y/MYCN cells here)[12]. In these cells a 24-hour doxycycline treatment induces a 9-fold increase in MYCN protein expression (Fig. S1A). We screened 3,526 compounds (Fig. S1B) measuring cell viability. Using a cutoff of 3-standard deviations of the median, we identified 77 hits that selectively affected the viability of MYCN induced SH-SY5Y/MYCN cells (Table S1). These hits included compounds that were previously shown to have activity in NB, e.g., gitoxin, a cardenolide glycoside, which inhibits the growth of NB cell lines in mice[13]; inhibitors of MEK, JAK and PI3-kinases, which compromise cell survival[14]; estradiol, which promotes differentiation[12, 15]; BH3-mimetics, which induce apoptosis[16, 17]; histone deacetylase inhibitors, which are emerging as promising treatments for NB[18-20]; the inosine monophosphate dehydrogenase inhibitor mycophenolate mofetil, which inhibits proliferation and survival of NB cell lines[21]; the Aurora kinase inhibitor AT9283, which was tested in phase 1 clinical NB trials[22]; and inhibitors of DNA methylation (decitabine and 5-azacytidine), which sensitize NB cells to chemotherapeutics[23].

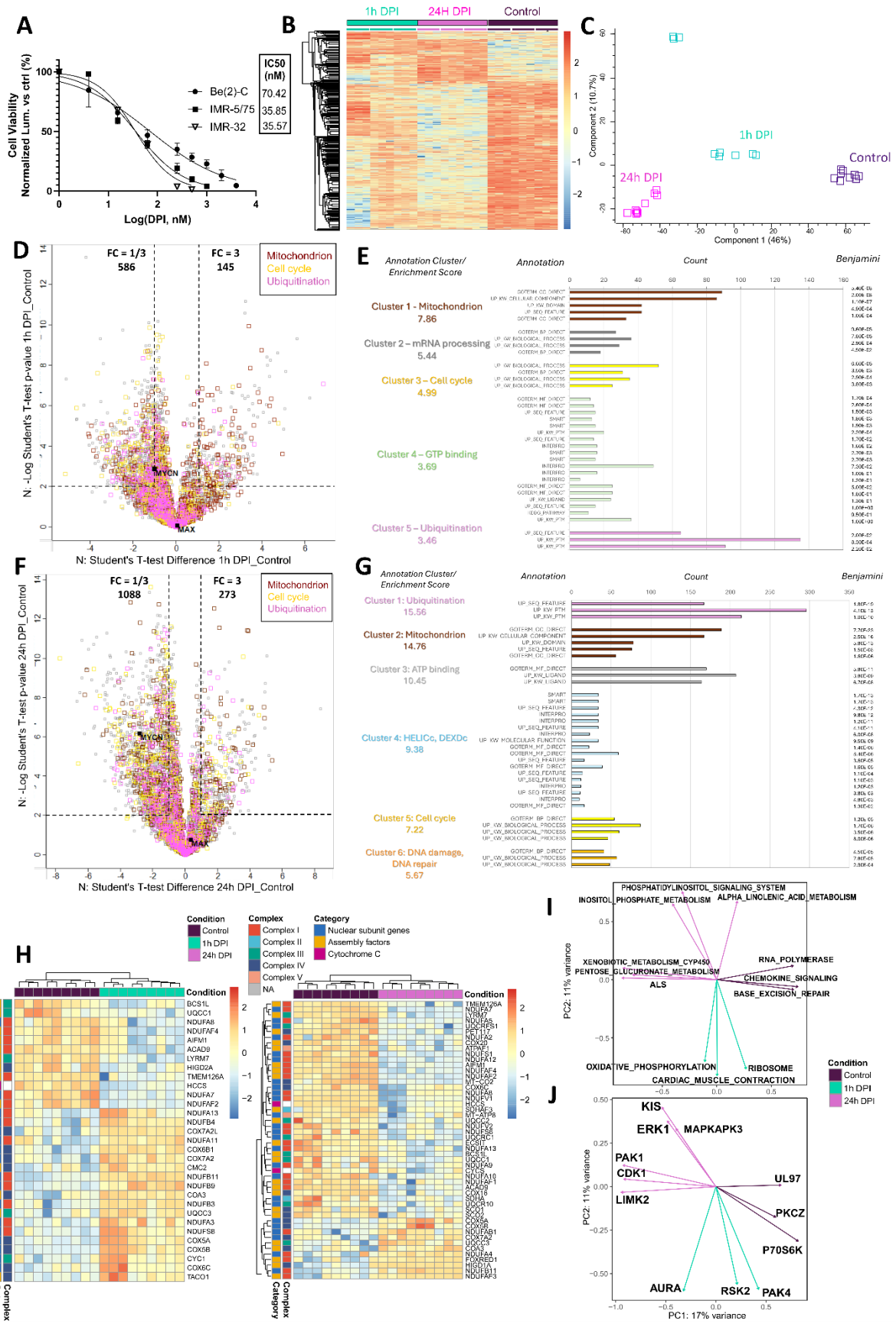

Figure 1. DPI decreases viability and triggers broad proteomic changes in MNA cells, notably affecting mitochondrial, cell cycle and ubiquitin-related protein networks. **(A)** Cell viability

was measured as loss of ATP content using CellTiter-Glo in 3 MNA cell lines, after 72h treatment with serial dilutions of DPI (0 - 4000 nM). **(B)** Hierarchical clustering of 2,907 differentially expressed (T-test significant) proteins in control and DPI-treated (1h and 24h 10 µM DPI) Be(2)-C cells. Each condition has 3 biological and 3 technical replicates. The values in the heatmap represent the Z-transformation of log2(LFQ intensity). Red: high protein expression; blue: low protein expression (FDR < 0.01). **(C)** PCA analysis using Benjamini-Hochberg FDR = 0.01. **(D)** Scatter plot, 1h DPI versus untreated control. A 3-fold change (FC) was taken as cut-off. **(E)** The top 5 clusters out of 113 clusters following functional annotation clustering of up- and downregulated proteins using DAVID default annotation categories. **(F)** Scatter plot, 24h DPI versus untreated control. A 3-fold change (FC) was taken as cut-off. **(G)** The top 6 clusters out of 204 clusters following functional annotation clustering of up- and downregulated proteins using DAVID default annotation categories. **(H)** Hierarchical clustering of differentially expressed (T-test significant, FDR > 0.01) mitochondrial proteins in control and DPI-treated (1h and 24h) Be(2)-C cells grouped by respiratory complex affiliation and annotated as nuclear-encoded subunits or assembly factors proteins. Each condition consists of 9 columns: 3 biological replicates, each loaded 3x on the mass spectrometer. **(I)** Integration of the whole proteomic and phosphoproteomic data. Pathways from the protein expression profiling data contributing to the shared sources of variation in the data. **(J)** The kinases from the phosphoproteomic data contributing to the shared sources of variation in the data. Vectors are coloured according to the condition they are associated with. (Mean ± SEM, n = 3).

To select a candidate for further investigation, we focused on compounds that demonstrated effective cell viability inhibition at low nanomolar concentrations, since such potency could allow lower clinical dosing and improve the therapeutic window (Fig. S1C). We further prioritized compounds with minimal reported genotoxicity and low systemic toxicity. Based on these criteria, we selected diphenyleneiodonium chloride (DPI) for detailed follow-up studies (Fig. S1D). Moreover, DPI was previously reported to protect SH-SY5Y cells against ROS induced cell death[24, 25], suggesting that DPI may offer a selective treatment of MNA NB. Therefore, we examined DPI in more detail, especially in respect to its increased potency on MNA cells.

To assess the inhibitory effects of DPI on other NB cells, cell viability was measured in the MNA Be(2)-C, IMR-5/75, and IMR-32 cell lines. DPI potently reduced cell viability in all three MNA cell lines, with IC_{50} values in the low nanomolar range (Fig. 1A). In addition, upregulating MYCN in SH-SY5Y/MYCN cells decreased the IC_{50} approximately 1.6-fold, whereas downregulating MYCN in IMR-5/75 cells (+Dox) increased the DPI IC_{50} more than 4-fold, indicating a MYCN-dependent contribution to DPI sensitivity, particularly pronounced in the MNA background (Fig. S1E-F).

Given the higher MYCN levels of Be(2)-C cells compared to other MNA lines (Fig. S1G), we selected this model to probe DPI's mechanism of action via mass spectrometry-based proteomic and phosphoproteomic profiling at 1h and 24h (Tables S2, S3). DPI profoundly

altered protein expression (Table S2). Of the 5,042 quantifiable proteins 2,907 (~57%) proteins were differentially expressed following DPI treatment (Fig. 1B). Principal component analysis (PCA) showed a clear separation of the three conditions (Fig. 1C). After 1 hour DPI treatment, 145 proteins were upregulated, and 586 proteins were downregulated threefold or more (Fig. 1D). Functional annotation clustering revealed that regulated proteins have functions related to mitochondria, mRNA processing, cell cycle, GDP-binding and ubiquitination (Fig. 1E). The GDP-binding cluster contains small G-proteins of the ARF, RAB and RAS families involved in vesicle transport and mitogenic signaling. After 24 hours DPI treatment, 273 and 1088 proteins were up- and downregulated, respectively (Fig. 1F). Cell cycle, mitochondria and ubiquitination remained the top altered functions. (Fig. 1G). Importantly, MYCN was downregulated by DPI treatment while the levels of MAX, a binding partner of MYCN remained unaffected.

Of the 3,860 quantifiable phosphosites, 1,384 were differentially abundant upon DPI treatment, following normalization to total proteome levels (Fig. S2A, Table S3). PCA analysis showed a clear separation of the three conditions (Fig. S2B). After 1h DPI treatment, 59 phosphorylation sites were upregulated and 28 were downregulated threefold or more (Fig. S2C). Functional annotation clustering mapped them to functions related to ubiquitination, RNA binding and mRNA processing (Fig. S2D). After 24 hours DPI treatment, 133 and 175 phosphorylation sites were up- and downregulated, respectively (Fig. S2E). Prominently altered functions included ubiquitination, nucleus, cell cycle, and translation initiation (Fig. S2F).

As the extensive changes in protein expression may influence the quantitation of phosphorylation sites, we integrated protein expression profiling with phosphoproteomics using multifactor analysis[26]. PCA analysis separated the conditions indicating that changes in both protein expression and phosphorylation independently contribute to the different molecular states induced by DPI treatment (Fig. S3A). The integrated data still discriminated the different treatment conditions revealing the shared sources of variation in the data represented by the factor loadings Z (Fig. S3B). The three conditions are mainly separated by Z1, while variations within conditions are mostly due to Z2. The biological processes and the phosphorylation changes associated with these variations were visualized by mapping the feature loadings onto pathways and kinases, respectively (Fig. 1I, J). These relationships provide information on the molecular mechanisms that mediate the DPI effects. For example, DPI treatment impacts oxidative phosphorylation and Aurora A (AURKA) kinase. Interestingly, in glioblastoma cells AURKA facilitates glycolysis, while suppressing OXPHOS[27]. DPI causes AURKA activation, albeit not significantly, (Fig. 1J, S3C), which could explain the similar effects of DPI on mitochondrial bioenergetics (Fig. 4B-D). The changes in inositol phosphate metabolism and phosphatidyl-signaling are correlated with increases in the activities of ERK1, KIS, and MAPKAPK3 (MK3) kinases after DPI treatment (Fig. 1I, J; S3C). ERK1 and KIS are involved in cell cycle progression, while MK3 promotes cell cycle arrest and senescence[28]. Pathways that characterize untreated control cells include pentose and glucuronate interconversion, which is involved in biosynthetic processes commonly upregulated in

193 cancer[29], and amyotrophic lateral sclerosis, which is hallmarked by dysfunctional
194 mitochondria[30]. Indeed, the corresponding kinases, PAK1, CDK1, and LIMK2 all have been
195 associated with mitochondrial dysfunction[31-33]. Their activities were upregulated by DPI
196 treatment (Fig. 1J, S3C). These results strongly suggested that mitochondria contain critical
197 targets for the DPI effects.
198
199 ***DPI induces MYCN degradation via phosphorylation-dependent proteasomal targeting***
200 Ubiquitin-mediated protein degradation was among the most significantly enriched pathways
201 in both total proteomic and phosphoproteomic analyses of MNA cells treated with DPI.
202 Importantly, phosphorylation of MYCN at threonine 58 (Thr58) and serine 62 (Ser62) has
203 previously been linked to its stability and degradation via the ubiquitin-proteasome
204 system[34]. At 24 hours post-DPI treatment, phosphorylation at both sites was significantly
205 decreased in the phosphoproteomic analysis (Fig. 2A), accompanied by a marked reduction in
206 MYCN protein levels in the total proteomics data (Fig. 2B). These findings were validated by
207 Western blotting (Fig. 2C). To determine whether reduced phosphorylation at these sites
208 facilitates MYCN degradation via ubiquitination, we pre-treated cells with the proteasome
209 inhibitor MG-132 prior to DPI exposure. MYCN protein levels were restored to baseline,
210 indicating that the DPI-induced loss of MYCN is proteasome-dependent (Fig. 2D). We then
211 performed a time-course analysis to assess whether MYCN loss was an early event following
212 DPI treatment. Both MYCN protein and phosphorylation levels were reduced as early as 30
213 minutes after DPI addition, suggesting a rapid post-translational regulatory mechanism (Fig.
214 2E). These changes were evident by Western blot and phosphoproteomics (Fig. 2A). Finally, a
215 dose-response experiment revealed that MYCN protein levels decreased in both MNA and
216 non-MNA cell lines, with the MNA cells showing higher sensitivity at lower DPI concentrations
217 (Fig. 2F).
218 Together, these results suggest that DPI promotes early MYCN degradation through a
219 mechanism involving reduced phosphorylation at regulatory residues and subsequent
220 proteasomal targeting. This effect is observed even in cells with lower basal MYCN expression,
221 indicating a shared vulnerability to DPI-induced destabilization of MYCN.

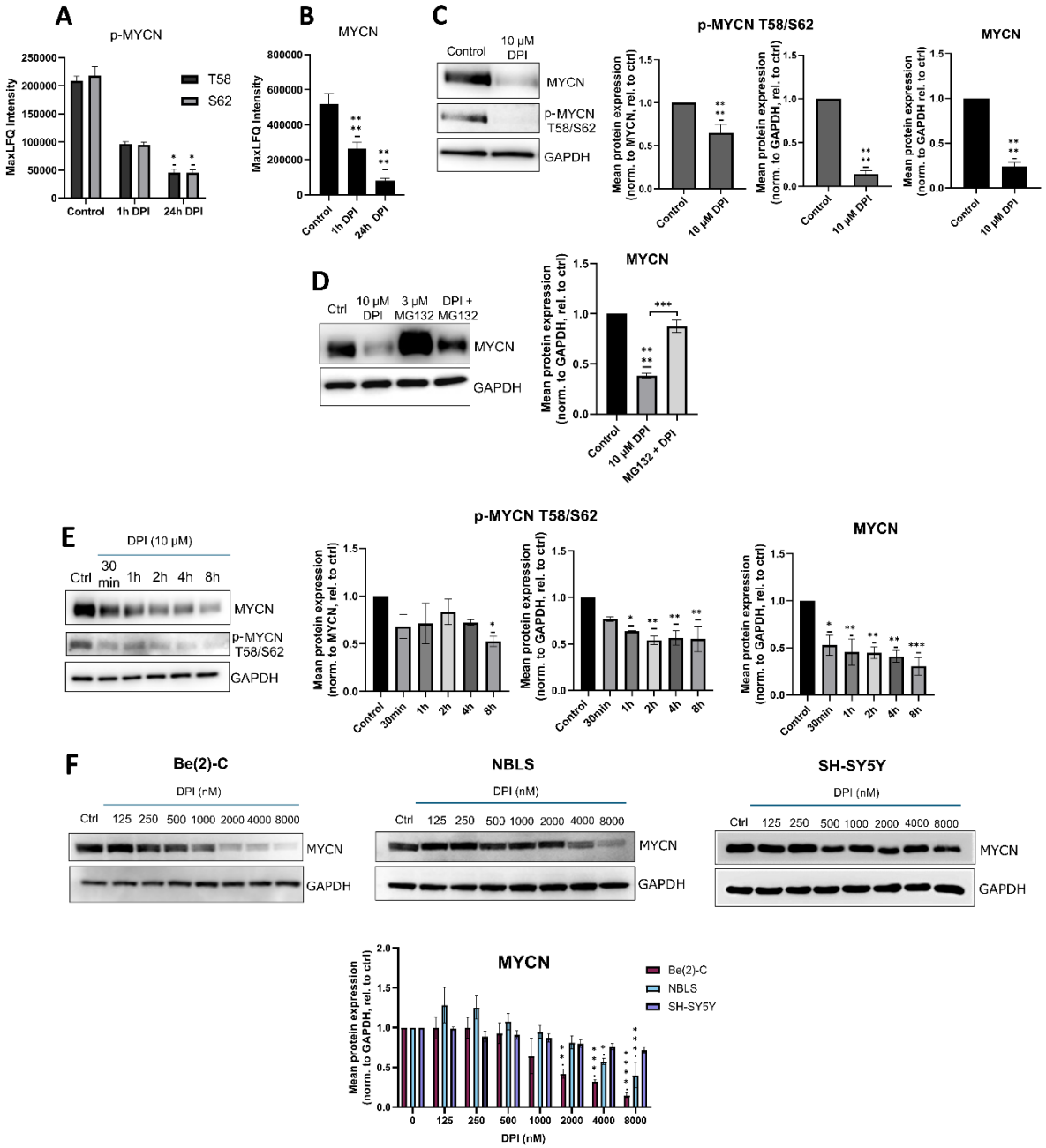

Figure 2. DPI affects MYCN phosphorylation status, impacting MYCN proteasomal degradation. **(A)** MYCN phosphorylation levels at Thr58 and Ser62 residues (p-MYCN) and **(B)** MYCN protein levels as measured by MS (Raw MaxLFQ Intensity) in Be(2)-C cells treated for 24h with 10 µM DPI (Significance indicated by stars is based on normalized data after statistical analysis). **(C–F)** Western blot analysis of p-MYCN (Thr58/Ser62) and/or total MYCN levels: **(C)** Validation of MS results in Be(2)-C cells treated with 10 µM DPI for 24 h. **(D)** MYCN levels following 4 h DPI treatment, after 1 h pre-treatment with 3 µM bortezomib. **(E)** Time-course treatment with 10 µM DPI for 30 min, 1 h, 2 h, 4 h, and 8 h. **(F)** Dose-response in Be(2)-C (MYCN-amplified), NBLS and SH-SY5Y (non-amplified) cells treated with serial DPI dilutions. GAPDH was used as a loading control for MYCN quantification. p-MYCN levels were normalized to both GAPDH and MYCN to confirm reproducibility. (Mean ± SEM, n = 3). Statistical

234 significance was assessed by one-way ANOVA ($p<0.05$ = *, $p<0.005$ = **, $p<0.0005$ = ***,
235 $p<0.0001$ = ****).
236
237 ***DPI affects mitochondrial encoded gene expression and mitochondrial superoxide-mediated***
238 ***apoptosis of MNA NB cells***
239 Our proteomics data in Be(2)-C cells showed that DPI alters the expression of ETC complex
240 components (Fig. 1H). These changes involved proteins encoded by nuclear as well as
241 mitochondrial DNA. To test whether DPI regulates gene expression on the transcriptional level
242 to change the composition of ETC complexes, we quantified the expression of mitochondrial
243 genes by RT-qPCR in a panel of DPI treated NB cells (Fig. 3A). DPI significantly reduced the
244 expression of most genes in MNA cells, i.e., KCN, KCNR and Be(2)-C (Fig. S1G). This effect was
245 attenuated or reversed in non-MNA NB cells (i.e., NBLS). Interestingly, DPI also downregulated
246 the expression of MYCN mRNA in MNA cells (Fig. 3A).
247 DPI significantly reduced the expression of mitochondrial encoded genes, particularly those
248 coding for complex I subunits (Fig. 3A). DPI was originally described as an NADPH oxidase
249 inhibitor, but in addition to flavin containing enzymes may also inhibit NAD/NADP-dependent
250 enzymes in the pentose phosphate pathway and tricarboxylic acid cycle[7]. DPI also can inhibit
251 complex I in the ETC but may selectively enhance superoxide production from forward
252 electron transport while blocking superoxide generation from reverse electron transport[8].
253 Superoxide dismutase decomposes the highly reactive superoxide to water and hydrogen
254 peroxide which is further detoxified by antioxidant enzymes, such as peroxiredoxins,
255 glutathione peroxidases, and catalases[35]. To selectively measure mitochondrial superoxide
256 production upon DPI treatment we used the MitoSOX Red indicator (Fig. 3B). DPI selectively
257 triggered superoxide production in the MNA cell lines, KCN, KCNR, and Be(2)-C, but not in the
258 non-MNA NBLS cells. DPI induced superoxide to similar levels as doxorubicin, which is thought
259 to exert cytotoxic effects in part via the generation of mtROS[36].
260 To further explore whether MYCN modulates mtROS production upon DPI treatment, we used
261 two MYCN-regulatable NB cell models: the MNA IMR-5/75 line, in which endogenous MYCN
262 expression can be downregulated by expression of a doxycycline inducible shRNA [37], and
263 the non-amplified SH-SY5Y/MYCN line, where MYCN overexpression can be induced from a
264 doxycycline inducible MYCN transgene. In IMR-5/75 cells, DPI significantly increased
265 mitochondrial superoxide levels regardless of MYCN downregulation (Fig. 3C). In contrast, in
266 SH-SY5Y/MYCN cells, DPI treatment did not augment mtROS levels, regardless whether MYCN
267 expression was induced or not (Fig. 3D). Additionally, MYCN induction or repression alone did
268 not significantly alter basal ROS levels in either model. These results suggest that high MYCN
269 expression sensitizes cells to ROS induced cell death (see below).
270 When excessively accumulated, ROS can trigger apoptotic pathways[38]. To assess whether
271 mtROS contribute to DPI-induced cell death, we pre-treated cells with the antioxidant N-
272 acetyl-cysteine (NAC) before DPI exposure and monitored cell death over a 72-hour period
273 (Fig. 3E). NAC treatment gradually rescued DPI-induced cell death in a time-dependent
274 manner, with a significant decrease in cytotoxicity observed as early as 24 hours (Fig. 3F).

Inhibited mitochondrial respiration may lead to cytochrome C release from the mitochondrial intermembrane space to the cytosol, leading to activation of caspase-9 and caspase-3 and subsequent apoptosis[39]. DPI caused cytochrome C release in Be(2)-C but not in NBL-S cells (Fig. S4A). Cytochrome C release correlated with caspase-9 and caspase-3 cleavage and activation (Fig. 3G, H). Indeed, in Be(2)-C cells, DPI induced a significant accumulation of cleaved caspase-9, along with an increase in cleaved caspase-3 levels, which were not present in NBLS.

These findings suggest that MNA confers a mitochondrial vulnerability, consistent with prior evidence that c-MYC can regulate the expression of ETC components[40]. To investigate whether high MYCN levels impact the composition of ETC complexes, we performed total proteomics comparing IMR-5/75 cells under MNA (−Dox), downregulated MYCN (+Dox), and DPI-treated conditions (Figs. 3I–K, S4B-I, Table S4). MYCN downregulation (+Dox) affected the expression of 24 nuclear-encoded mitochondrial proteins (Fig. 3I). DPI treatment in −Dox cells altered 26 nuclear-encoded mitochondrial proteins and one mitochondrially encoded subunit (Fig. 3J). Notably, 10 of the proteins downregulated by DPI overlapped with those affected by MYCN downregulation, all regulated in the same direction. Moreover, both MYCN downregulation and DPI treatment downregulated TFAM and TFB1M, key mitochondrial transcription factors. In contrast, DPI treatment in +Dox cells led to significant changes in only three nuclear-encoded mitochondrial proteins, one of which was also affected by MYCN downregulation (Fig. 3K). Interestingly, ChIP-seq data from MNA NB cells (GSE183641) show that MYCN binds the promoter regions of NDUFAF4 and COA7 (Fig. S5). The expression of these proteins decreased ~3-fold and ~8-fold, respectively, upon MYCN knockdown, supporting their direct regulation by MYCN (Fig. 3I,J). The expression of these two proteins was also downregulated by DPI (Fig. 3I,J). Importantly, pathway enrichment analysis of DPI-treated IMR-5/75 -Dox cells revealed similar pathways to those observed in Be(2)-C cells (Figs. 1E, G; S4F, G), suggesting translational effects of DPI across different MNA cell lines.

Together, these data suggest that DPI disrupts mitochondrial-encoded gene expression in MNA cells, particularly complex I, creating a vulnerability to mtROS-induced apoptosis via cytochrome c release and caspase activation. This supports that DPI-induced cell death in MNA cells is at least partially mediated by ROS accumulation. While high MYCN expression appears to sensitize cells to ROS, acute MYCN up- or downregulation in the doxycycline regulatable cell lines does not significantly affect ROS generation (Fig. 3C,D) suggesting that ROS generation is not directly controlled by MYCN. However, an indirect effect is plausible. Our proteomic analysis in a MYCN-regulatable cell system indicates that high MYCN levels alter the composition of all ETC complexes (Fig. 3I). These changes may promote ROS production and may persist after acute regulation of MYCN expression. Interestingly, DPI can partially reverse the changes in ETC composition. This finding is also observable on a more global level, as pathways enriched upon MYCN downregulation closely mirror those affected by DPI treatment (Fig. S4C, E). Altogether, these findings support a MYCN-driven mitochondrial dependency that underlies the enhanced sensitivity of MNA cells to DPI.

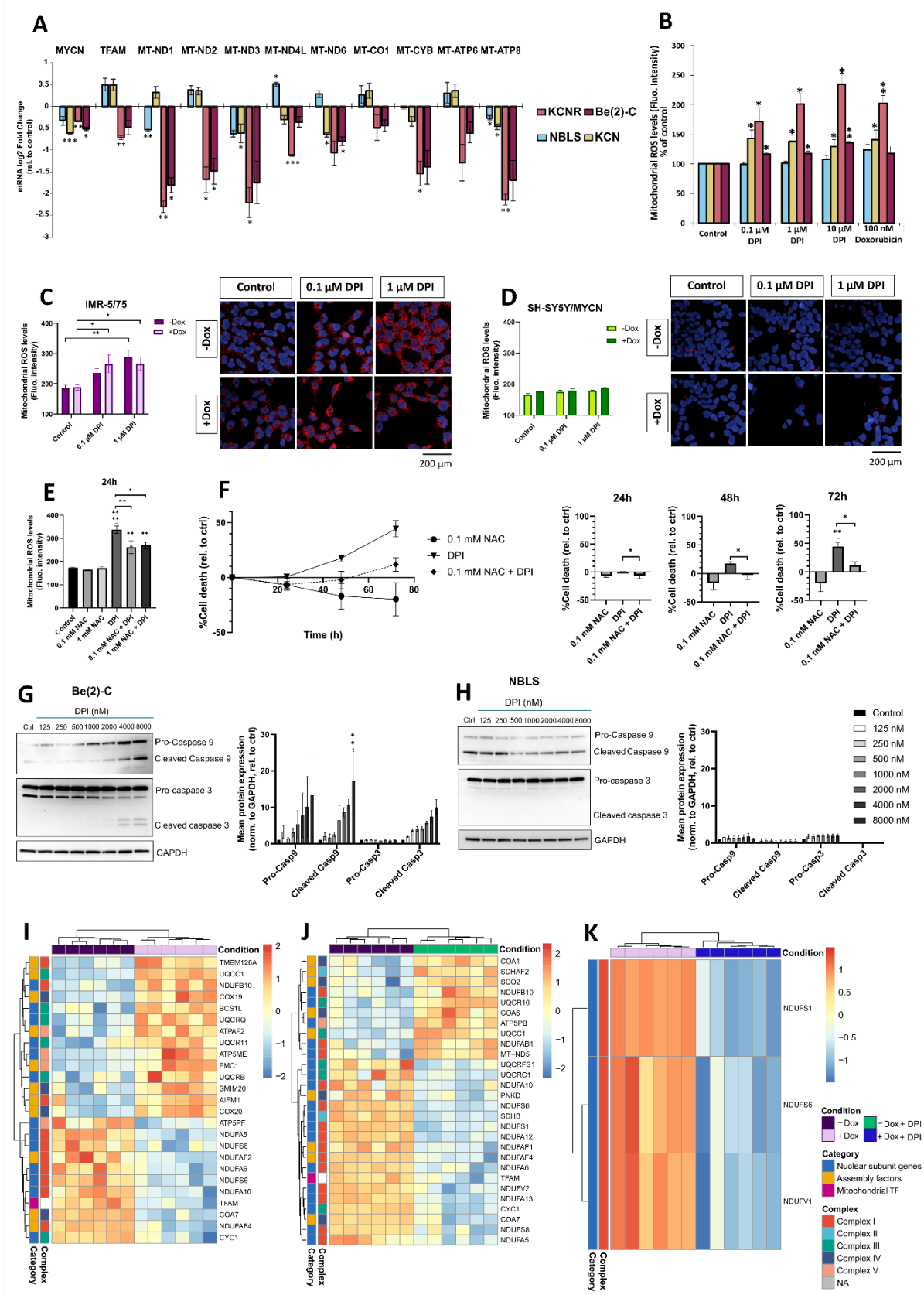

Figure 3. DPI targets mitochondrial gene expression and induces mtROS-dependent apoptosis in MYCN-amplified neuroblastoma cells. **(A)** RT-qPCR analysis of mitochondrial-encoded genes and MYCN in NBLS, KCN, KCNR, and Be(2)-C cells after DPI treatment (1 µM,

24h), shown as fold change over control. **(B)** Mitochondrial superoxide levels in NB cell lines treated with DPI for 24h, measured by MitoSOX Red-based flow cytometry. Doxorubicin (100 nM) used as positive control. **(C, D)** MitoSOX Red-based confocal imaging of mtROS in IMR-5/75 ±Dox **(C)** and SH-SY5Y/MYCN ±Dox **(D)** treated with DPI for 24h. **(E)** mtROS levels in Be(2)-C cells treated with NAC (0.1 or 1 mM) alone or 1 h prior to DPI (5 µM, 24h), measured by MitoSOX Red confocal imaging. **(F)** Cell death in Be(2)-C cells treated with NAC (0.1 or 1 mM) alone or 1h prior to DPI (5 µM, 24, 48, and 72h) measured with the CellTox Green indicator. **(G, H)** Western blot analysis of cleaved and pro-caspase-3 and -9 in Be(2)-C **(G)** and NBLS **(H)** cells after 24h DPI treatment (serial dilutions: 125–8000 nM). GAPDH was used as a loading control. **(I–K)** Hierarchical clustering of significantly altered mitochondrial proteins (T-test significant, FDR < 0.01) identified by MS-based proteomics in IMR-5/75: +Dox vs -Dox **(I)**, DPI-treated vs -Dox control **(J)**, and +Dox DPI-treated vs +Dox control **(K)**, organized by ETC complex and category. Each condition consists of 9 columns: 3 biological replicates, each loaded 3x on the mass spectrometer. (Mean ± SEM; n=3; *p < 0.05, **p < 0.01, ***p < 0.001, p<0.0001 = ****; Two-sample T-test, Ordinary One-Way ANOVA or Two-Way ANOVA).

DPI modulates ATP production and promotes cell death, with MYCN amplification enhancing sensitivity

The substantial changes in the expression of ETC complex proteins mediated by MYCN and DPI likely affect mitochondrial functions. Therefore, we measured ATP production in the NB cells with regulatable MYCN using a Seahorse Analyzer (Fig. 4A-D). ATP can be produced by OXPHOS in the mitochondria or by glycolysis in the cytosol. Total ATP production was higher in IMR-5/75 than in SH-SY5Y/MYCN cells, but DPI reduced it in IMR-5/75 while slightly elevating it in SH-SY5Y/MYCN cells, although not in a significant manner (Fig. 4A). Interestingly, in IMR-5/75 more ATP (~60%) was produced through OXPHOS than glycolysis in basal conditions, while the ratio was reversed in SH-SY5Y/MYCN cells (Fig. 4B-D). DPI robustly suppressed mitochondrial ATP production in IMR-5/75 and only non-significantly in SH-SY5Y/MYCN (Fig. 4C). Glycolytic ATP production was significantly enhanced by DPI in both cell lines, probably as a compensatory mechanism (Fig. 4D). Regulating MYCN levels only had a small, non-significant impact.

To further characterize the impact of DPI in a MYCN-regulatable context, we assessed cytotoxicity. While total ATP production was not significantly affected by DPI after 24 hours (Fig. 4A), prolonged exposure led to marked reductions in cell viability, as measured by loss in ATP content, after 72 hours (Fig. S1E-F). A time-course analysis of cytotoxicity revealed effects as soon as 24 hours post-treatment, with increasing differences between MYCN-high and MYCN-low conditions at 48 and 72 hours in both cell lines (Fig. 4E, F). Notably, the MNA IMR-5/75 cells were overall more sensitive to DPI than the non-MNA SH-SY5Y/MYCN cells, and MYCN modulation significantly influenced the extent of cell death in both models. For instance, at 72 hours, 1 µM DPI induced ~75% cell death in MYCN-high IMR-5/75 (-Dox) cells compared to ~40% in MYCN-low (+Dox) cells (Fig. 4E, F).

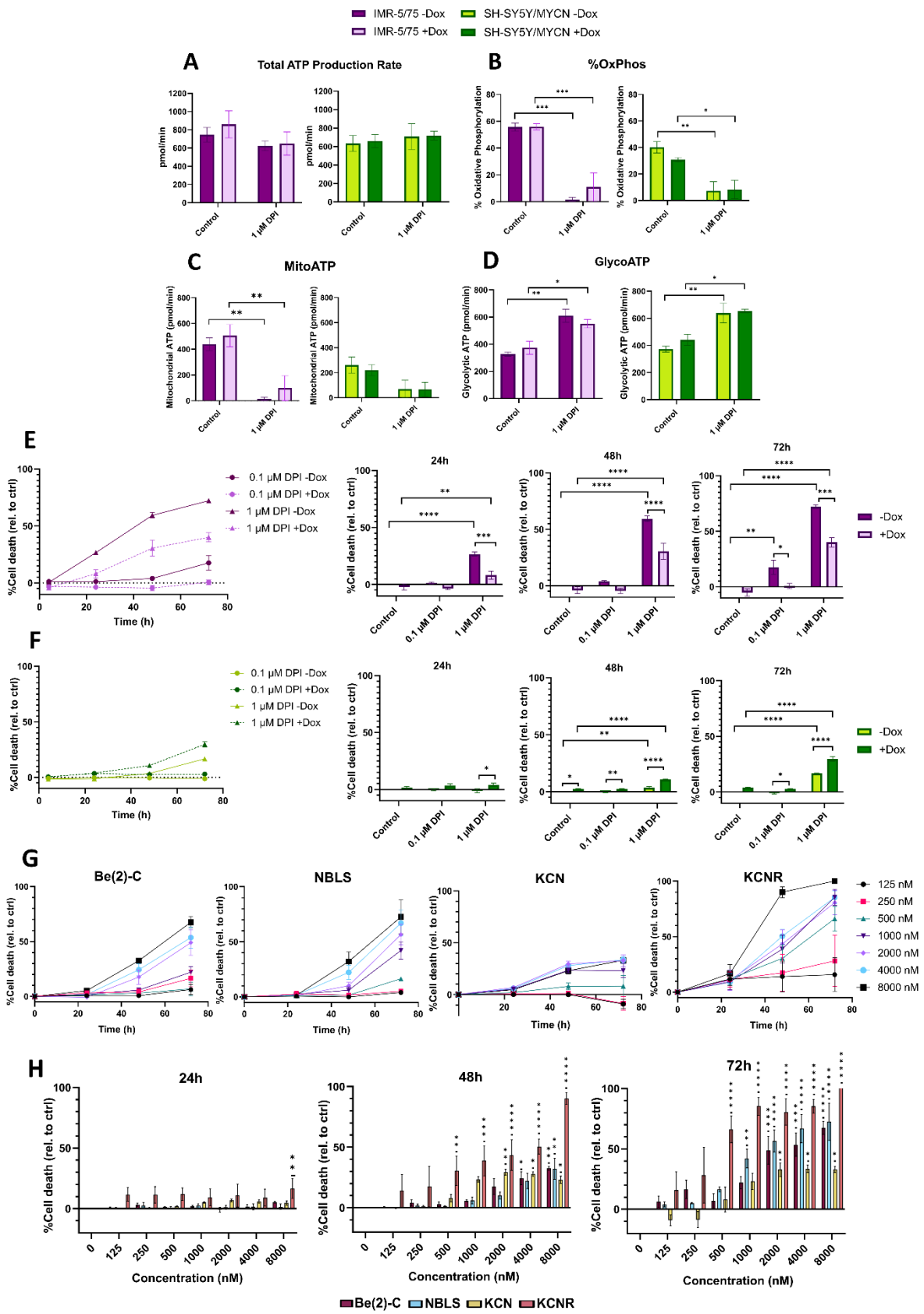

Figure 4. DPI reduces mitochondrial ATP production and promotes cell death in NB cells, with increased vulnerability in MNA cells. **(A)** Total ATP production rate, **(B)** percentage of ATP derived from OXPHOS, **(C)** mitochondrial ATP production, and **(D)** glycolytic ATP production

measured in IMR-5/75 and SH-SY5Y/MYCN cells ±Dox and ±DPI (1 µM, 24h) using a Seahorse XFe24 Analyzer. **(E, F)** Cytotoxicity measured by CellTox Green (loss of membrane integrity) in IMR-5/75 **(E)** and SH-SY5Y/MYCN **(F)** cells treated with 0.1 or 1 µM DPI ±Dox over 72h. **(G, H)** Cell death assessed by CellTox Green in Be(2)-C, NBLS, KCN, and KCNR cells treated with DPI (0–8000 nM) over 72 h. (Mean ± SEM; n=3; *p < 0.05, **p < 0.01, ***p < 0.001, p<0.0001 = ****; Two-Way ANOVA).

To compare these effects across NB cell lines with distinct genetic backgrounds, we next assessed cell death kinetics in Be(2)-C, NBLS, KCN, and KCNR cells treated with serial dilutions of DPI (Fig. 4G, H). While non-MNA NBLS cells were also susceptible to DPI, they required higher concentrations and longer exposure times to induce comparable levels of cell death. Notably, the KCNR cell line, which is derived from a relapsed tumour after chemotherapy from the same patient as the KCN line, was most sensitive to DPI. This was particularly evident when compared to the treatment-naïve KCN cells, suggesting that treatment history and acquired vulnerabilities may enhance sensitivity to mitochondrial perturbation.
These results indicate that DPI selectively impairs mitochondrial ATP production in MNA IMR-5/75 cells, which rely more heavily on OXPHOS, while having limited impact on the more glycolytic SH-SY5Y/MYCN cells. The increased glycolytic ATP observed in both cell lines upon DPI treatment likely reflects a compensatory metabolic shift. This metabolic vulnerability is accompanied by enhanced sensitivity to DPI-induced cytotoxicity, particularly in MNA cells, supporting a MYCN-linked mitochondrial dependency that contributes to cell death.

DPI counteracts the malignant phenotype of NB cells

The hallmarks of malignant transformation include resisting cell death and maintaining proliferation at the cost of differentiation[41]. MYCN promotes an undifferentiated, proliferative state in NB by actively repressing neuronal differentiation programs[42]. To assess the impact of DPI on these traits we carried out a soft agar colony forming assay and a differentiation experiment. Colony forming assays test the ability of single cells to survive and proliferate into a colony, which are typical properties of cancer cells[43]. The ability to form colonies decreased with lower MYCN expression levels, but DPI completely suppressed colony formation in all NB cells tested (Fig. S6A).
We further assessed differentiation through analysis of neuronal markers, neurite length and % of differentiating cells in IMR-5/75 and SH-SY5Y/MYCN cells ±Dox (Fig. 5A, B). For this, we compared DPI to retinoic acid (RA), which is a clinically used differentiation agent for neuroblastoma[44]. RA and even more DPI treatment significantly increased expression of the differentiation marker tyrosine hydroxylase (TH) after 5 days in IMR-5/75 cells, an effect reduced upon MYCN downregulation (+Dox) in DPI, but not RA treated cells (Fig. 5A). In SH-SY5Y/MYCN cells, DPI also moderately increased TH levels independently of MYCN induction. DPI treatment robustly decreased MYCN expression in IMR-5/75 cells and also in SH-SY5Y/MYCN when MYCN expression was induced. This observation is consistent with the notion that DPI has bigger effects when MYCN levels are higher. Morphological analysis

404 revealed increased neurite length in IMR-5/75 cells treated with DPI, independent of MYCN
405 levels (Fig. 5B). In contrast, RA increased neurite length significantly only when MYCN was
406 knocked down. In SH-SY5Y/MYCN DPI has little effect, whereas RA only augmented neurite
407 length when MYCN expression was induced, suggesting that RA has the best effects when
408 MYCN is moderately overexpressed. This pattern was confirmed when quantifying the number
409 of morphological differentiated cells, with the exception that DPI increased the % of
410 differentiating cells solely in SH-SY5Y/MYCN cells upon MYCN overexpression, and that RA was
411 more efficient than DPI.
412 To complement these findings, we analysed proteomics data from DPI-treated Be(2)-C and
413 IMR-5/75 -/+Dox cells using a curated NB pluripotency signature to assess whether DPI could
414 shift cells from a pluripotent to a differentiated state[45, 46] (Figs. 5C, D). Indeed, DPI caused
415 a loss of this signature, indicating a global shift towards differentiation. Interestingly, in IMR-
416 5/75 cells, the analysis confirmed that DPI induced a more substantial loss of pluripotency in
417 cells with higher MYCN levels (Fig. 5D). Together, these results suggest that DPI can counteract
418 malignant properties of NB cells through both MYCN-dependent and independent
419 mechanisms, with more pronounced effects when MYCN is increased (Fig. S6C).

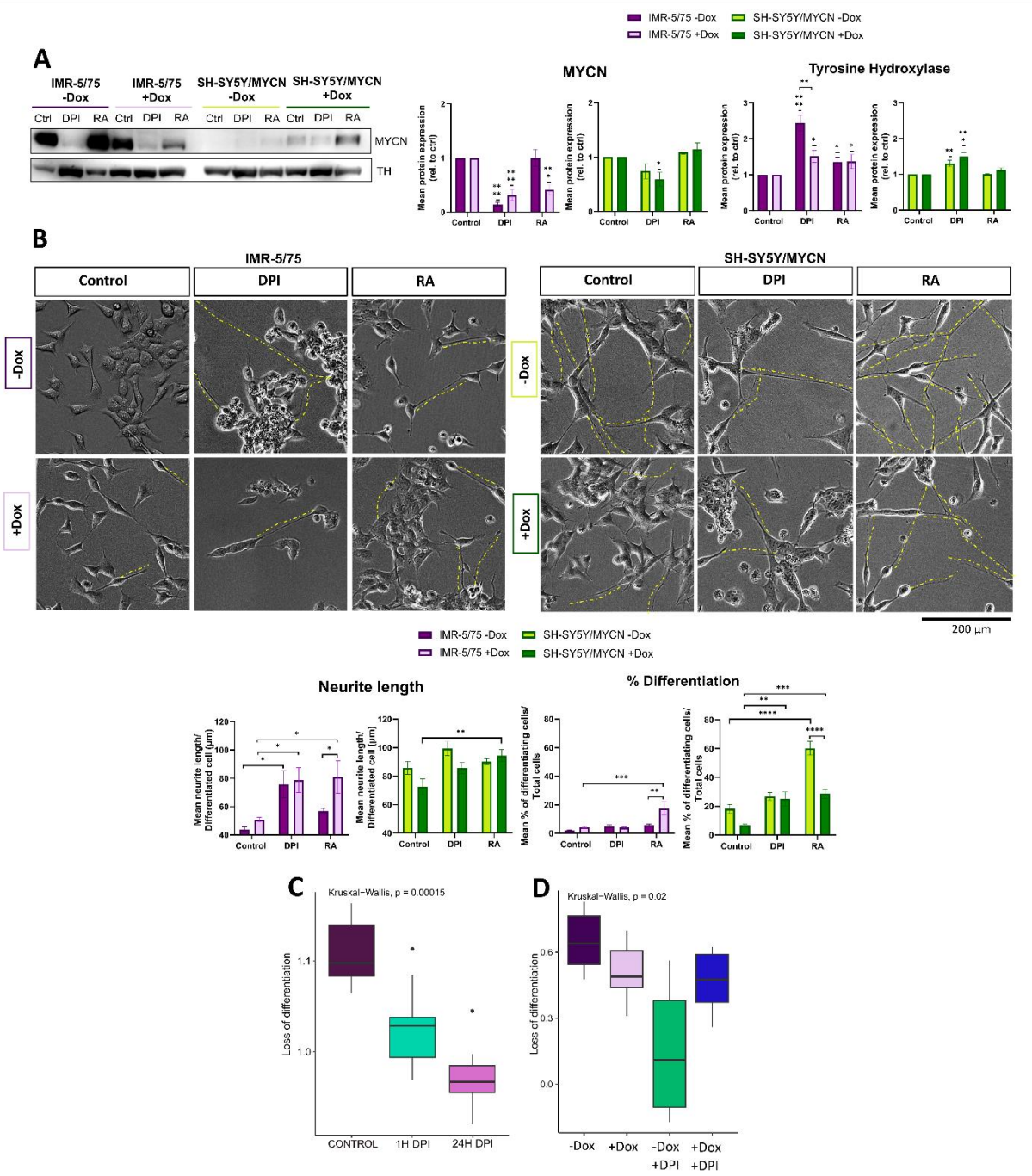

Figure 5. DPI induces differentiation of NB cells. IMR-5/75 and SH-SY5Y/MYCN cells were treated with -/+Dox and 0.5 µM DPI, 10 µM RA, or vehicle for 5 days. **(A)** Protein levels of the neuronal differentiation marker tyrosine hydroxylase (TH) and the pluripotency marker MYCN were assessed by Western blot. As these treatments disrupted traditional loading controls after 5 days, they could not be used for normalization. Equal loading was verified by BCA assay, and Coomassie Blue staining of membranes is shown in Supplementary Figure S6B as a control for total protein. **(B)** Neurite outgrowth and percentage of differentiating cells were quantified by microscopy. Cells with neurites ≥ 2 cell body diameters were considered differentiated. Three random fields per condition were analyzed from three independent experiments. Dotted yellow lines were used to outline neurite extensions indicative of neuronal

differentiation. **(C, D)** Expression of a curated pluripotency-associated NB signature (BMI1, FN1, IGFBP2, MYCN, NES, NGFR, VIM) in **(C)** Be(2)-C cells treated with 10 µM DPI for 24 h and (D) IMR-5/75 -/+Dox cells treated with 0.5 µM DPI for 24 h based on MS-proteomic analysis. (Mean ± SEM; n=3; *p < 0.05, **p < 0.01, ***p < 0.001, p<0.0001 = ****; One-Way ANOVA on ranks; Two-Way ANOVA, Kruskal-Wallis test).

DPI inhibits NB growth and metastatic spread in zebrafish models of NB

To test whether DPI is also active against *in vivo* tumors, we used a well characterized zebrafish model of MYCN-driven NB. These fish overexpress an EGFP-MYCN transgene in the fish-equivalent of the adrenal gland and spontaneously develop NBs that faithfully recapitulate the genetic and molecular features of human MNA NB[47-51]. Administration of DPI (1 µM) to tumor bearing fish was non-toxic and resulted in a significant tumor regression after two weeks of treatment (Fig. 6A).

To assess whether tumors formed by human NB cells are also susceptible to DPI, we transplanted fluorescently labelled Be(2)-C cells into the perivitelline space of 2 days old zebrafish embryos and observed them over 72 hours (Fig. 6B, C). The transplants grew and spread throughout the fish. DPI treatment (1 µM) significantly reduced the primary tumor mass and number of micrometastases in the tail of zebrafish larvae compared to the non-treated group.

These findings show that DPI is effective against endogenously arising and transplanted NB suggesting that complex I inhibitors could be developed into a non-genotoxic treatment for NB.

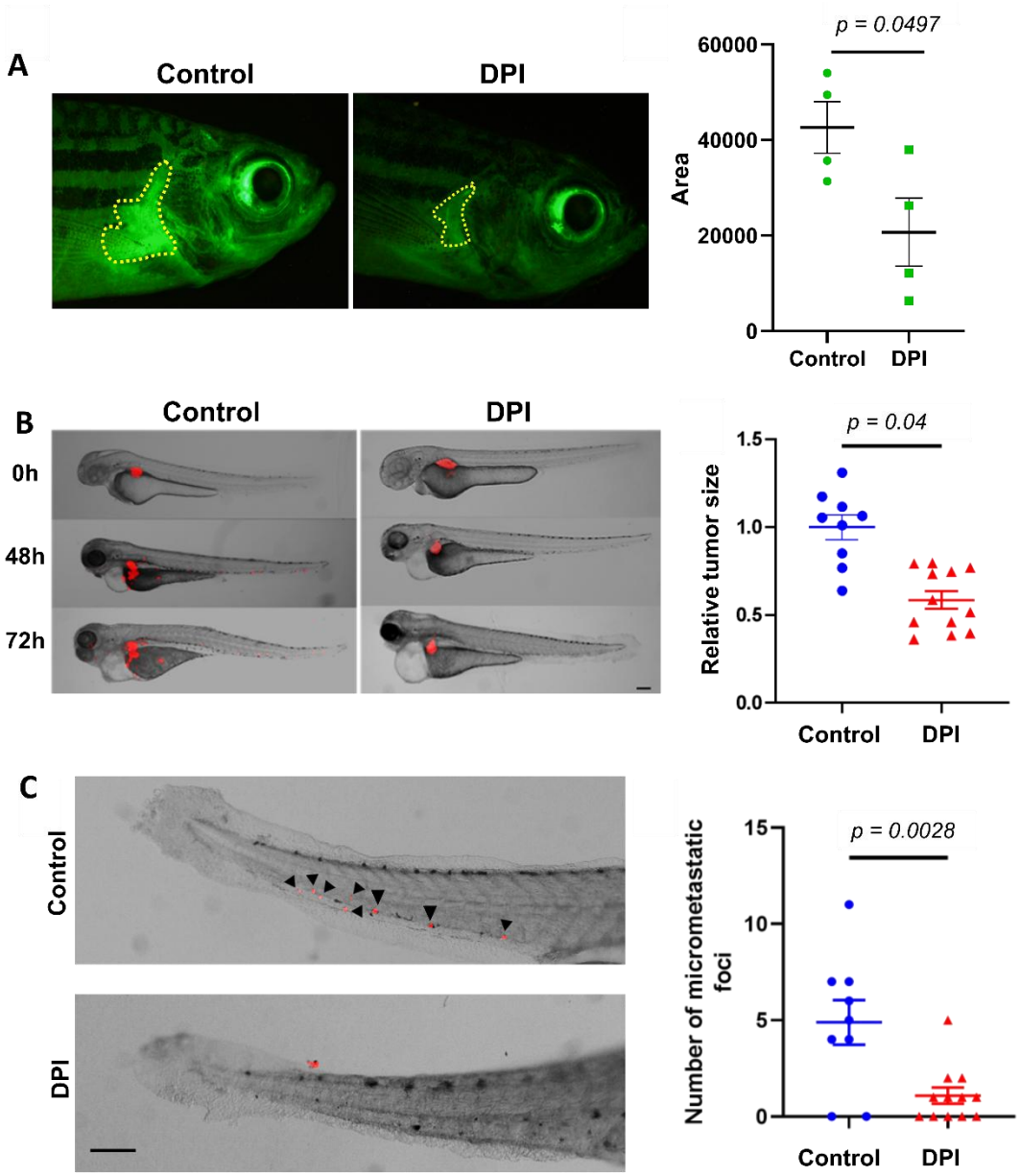

Figure 6. DPI suppresses tumor growth and metastatic spread in zebrafish models of MNA neuroblastoma. **(A)** Neuroblastoma growth in a zebrafish model driven by the overexpression of EGFP-MYCN. Tumor bearing fish (15 months of age) were treated with dimethyl sulfoxide (DMSO) control or DPI (1 µM, 14 days). Tumors (marked by broken yellow lines) are easily visualized due to EGFP-MYCN expression, and their sizes were determined by quantifying green fluorescence. (Mean ± SEM, Two-sample t-test, n = 4). **(B)** Be(2)-C cells labeled with red fluorescent dye were injected into the perivitelline space of 2 days post fertilization zebrafish embryos and treated with DPI (1 µM) for 72 hours. Tumor size was quantified by measuring red fluorescence. (Mean ± SEM, Two-sample t-test). **(C)** Black arrowheads indicate micro-metastatic foci in the tail of the fish. (Mean ± SEM, Two-sample t-test). Scalebars = 100 µm.

468 **Discussion**

469 Our results suggest that DPI is a promising tool compound for the development of new non-
470 genotoxic NB treatments targeting complex I. Although we observed no toxicity in our
471 zebrafish experiments, the use of DPI at micromolar concentrations may be limited by toxicity
472 in mammalian species[52]. Therefore, to develop a clinically relevant drug, it is important to
473 understand the mode of action, especially how DPI selectively targets biological processes
474 specific to high-risk NB cells. While DPI was originally discovered as NADPH oxidase inhibitor,
475 it transpired that it affects many more targets[7]. Our findings indicate that most of the
476 relevant DPI actions are related to cells with MYCN gene amplification.

477 While MYCN is clearly a driver gene of high-risk NB, exploiting it as drug target has remained
478 largely elusive[4]. MYCN itself seems not druggable as it has no obvious hydrophobic pockets
479 where small molecule inhibitors can bind. Therefore, indirect approaches have prevailed. For
480 example, Aurora A (AURA) kinase binds to MYCN and protects it from degradation. Aurora A
481 kinase inhibitors (AURAi) destabilize this interaction causing MYCN degradation[53]. They
482 showed promising results in preclinical models but proved ineffective in clinical trials in
483 humans[54]. Recent improvements combined AURAi with ATR kinase inhibitors, exploiting the
484 fact that MYCN activates AURA, and AURA inhibition induces DNA damage that requires ATR
485 kinase for repair[55]. Thus, inhibiting both AURA and ATR prevents MYCN from limiting DNA
486 damage. This mechanism is interesting, as according to our proteomics data DNA repair is an
487 enriched pathway, and DPI treatment reduced the expression of ATR to 29% within 24 hours.
488 Aurora A levels also diminished, albeit to a lesser extent, to 64%. These changes could
489 plausibly contribute to both the decrease in MYCN protein and the enhanced apoptosis in
490 response to DPI.

491 DPI also modulates the phosphorylation sites of MYCN that regulate its activation and
492 subsequent degradation, namely T58 and S62[56]. Mitogenic kinases (CDK1, ERK1/2, mTOR)
493 phosphorylate S62 enhancing MYCN activity, while the subsequent phosphorylation of T58
494 induces S62 dephosphorylation and MYCN degradation. Our normalized phosphoproteomics
495 data show that DPI decreases the phosphorylation of MYCN at T58 and S62. In addition, DPI
496 also reduces the phosphorylation of S371 and S375 after 24 hours. The corresponding
497 phosphorylation sites in c-MYC, S344 and S348, inhibit both the transcriptional and
498 transforming activity of c-MYC[57]. Thus, DPI may control MYCN activity and stability by
499 multiple mechanisms. Interestingly, the extent of MYCN reduction by DPI correlated with
500 MYCN status suggesting that the suppressive mechanism is under control of MYCN itself. Our
501 previous results showed that MYCN regulates the expression of its own interaction
502 partners[12], and analyzing the impact of DPI on the expression of MYCN interaction partners
503 could provide further insights into how DPI preferentially impacts overexpressed MYCN.
504 Interestingly, we found that MAX expression remained unchanged upon DPI treatment,
505 suggesting that MYCN and MAX might be regulated independently under specific stress
506 conditions. Using MYCN-regulatable cell lines and a panel of NB cell lines with diverse MYCN
507 status and genetic backgrounds, we showed that DPI preferentially targets cells with MNA but
508 also affects non-MNA cells at higher doses and longer exposure times. This highlights DPI's

509 broader therapeutic potential.
510 Apart from these effects on MYCN itself, DPI overlaps with MYCN in affecting the function of
511 mitochondria. MNA fundamentally changes the metabolic functions of mitochondria[58] and
512 renders MNA cells dependent on MYCN to maintain the function of these altered
513 mitochondria[58]. Our proteomics profiling revealed profound changes in the expression of
514 mitochondrial ETC proteins, which likely would modify the composition and function of ETC
515 complexes. Amplified MYCN can increase both glycolysis and OXPHOS[58]. Using Seahorse
516 analysis, we found that MNA cells preferentially use mitochondrial ATP generated through
517 OXPHOS. DPI profoundly suppresses OXPHOS while triggering a compensatory increase in
518 glycolysis, possibly leading to metabolic imbalance. This metabolic shift likely represents an
519 adaptive response, yet it is insufficient to prevent DPI-induced cytotoxicity.
520 As DPI can inhibit ETC complex I in the OXPHOS chain leading to the production of
521 superoxide[8], the generation of ROS induced by DPI in MNA cells is likely closely related to
522 this metabolic imbalance. DPI was reported to scavenge ROS[24, 25], but the altered
523 composition of ETC complexes in MNA cells may subvert this protective function into a
524 deleterious liability. In our experiments, DPI induced superoxide production, caspase-
525 dependent apoptosis, cytotoxicity, differentiation, and decreased proliferation and MYCN
526 levels more strongly in MNA cells. While DPI also reduced cell viability and increased cell death
527 in non-MNA cells, this required higher concentrations and longer exposure times. Although
528 ROS levels were not directly modulated by MYCN regulation alone, compensatory
529 mechanisms may buffer this effect. However, under DPI-induced complex I stress, these
530 compensatory mechanisms might become overwhelmed, pushing ROS beyond a critical
531 threshold that triggers cell death particularly in MNA cells. In our experiments the ability of
532 DPI to induce superoxide production, apoptosis, cytotoxicity and decrease of proliferation was
533 linked to higher MYCN levels. The only biological DPI effect that was MYCN independent, was
534 the induction of differentiation. Thus, it seems that the most relevant targets of DPI that
535 suppress MNA NB reside in the mitochondria exerting the metabolic imbalance and
536 superoxide production induced by MYCN amplification.
537 Although mitochondria are moving into the limelight as targets for new cancer drugs[59], a
538 wealth of previous experience shows that monotherapies are unlikely to succeed in the clinic.
539 Therefore, complex I inhibitors will need to be combined with other drugs. Our results suggest
540 that DPI synergizes with chemotherapeutic drugs currently used for NB treatment, such as
541 vincristine, and also with agents that modulate mitochondrial ROS production[60]. Taken
542 together, these data indicate that the MYCN dependent metabolic alterations are the most
543 relevant DPI target for further drug development.
544
545 **Methods**
546 ***Cell lines.*** Cells were generous gifts from J Schulte (Charite, Berlin, Germany) and F
547 Westermann (DKFZ, Heidelberg, Germany). SH-SY5Y and NBLS (single MYCN gene copy) and
548 KCN, KCNR, Be(2)-C (MNA) cells were cultured in RPMI-1640 (Gibco), supplemented with 10%
549 fetal bovine serum (Gibco), 2 mmol/L L-glutamine (Gibco), and 1% penicillin-streptomycin

550 solution (Gibco). For SY5Y/6TR (EU)/pTrex-Dest-30/MYCN cells (here called SH-SY5Y/MYCN
551 cells), where MYCN overexpression is doxycycline inducible[12], the above culture media was
552 supplemented with Blasticidin (7.5 µg/mL) and G418 (200 µg/mL). For the MYCN-amplified
553 IMR-5/75 cells, where MYCN is downregulatable by doxycycline induction of an shRNA against
554 MYCN[37], the culture media also contained Blasticidin (5 µg/mL) and Zeocin (50 µg/mL).
555 Doxycycline was used at 1 µg/mL concentration.
556
557 ***Drug screen.*** SH-SY5Y/MYCN cells were seeded in 384-well plates (1500 cells per well) and
558 treated with 1µg/ml Doxycycline (Sigma) for 24 hours, which resulted in a 11-fold increase in
559 MYCN mRNA. Then, uninduced and Doxycycline induced cells were treated with the following
560 drugs: Biomol (80 known kinase and phosphatase inhibitors; at 10, 1, 0.1 and 0.01 µmol/L),
561 LOPAC (1280 compounds; at 1 and 0.1 µmol/L), Microsource Cancer (80 compounds) and
562 Microsource Spectrum (2000 compounds including most of the known drugs and other
563 bioactive compounds and natural products; 1 and 0.1 µmol/L) totaling 3500 compounds
564 (Table S1). Viability was measured 76 hours later using the CellTiter-GLo Luminescence Cell
565 Viability Assay as described previously[12].
566
567 ***Chemicals.*** Diphenyleneiodonium chloride (DPI) was purchased from Enzo Life Sciences
568 (#BML-CN240-0010). Dimethyl sulfoxide (DMSO, vehicle) (#D2650), MG-132 (#M7449) and
569 retinoic acid (#R2625) were from Merck. Doxorubicin was purchased from Selleck Chemicals
570 (#S1225).
571
572 ***Western blotting.*** Cells were lysed with lysis buffer (1% Triton X, 150 mM NaCl, 1 mM $MgCl_2$,
573 and 20 mM Tris–HCl, pH 7.5) supplemented with Complete Mini (Roche) protease and
574 PhosStop (Roche) phosphatase inhibitors. Proteins were resolved in 10% NuPAGE Bis-Tris
575 Mini gels (Life technologies) at 100 V and transferred to a polyvinylidene difluoride membrane
576 (Invitrolon) at 30 V, 70 min. Membranes were blocked using 5% non-fat dried milk (Sigma) in
577 TBS with 0.05% Tween (TBS-T) for 1 h and incubated overnight at 4°C with primary antibodies
578 against MYCN (#sc-53993, Santa Cruz), p-MYCN Thr58/Ser62 (#9401, Cell Signaling), GADPH
579 (#2118, Cell Signaling), cytochrome C (#Ab110325, Abcam), caspase 3 (#9665, Cell Signaling),
580 caspase 9 (#9508, Cell Signaling), tyrosine hydroxylase (#2792, Cell Signaling) diluted in 1:1000
581 in 5% BSA/TBS-T. Membranes were then washed with TBS-T and incubated for 1 h at room
582 temperature with peroxidase conjugated anti-mouse or anti-rabbit IgG (1:5000 dilution, 7076
583 and 7074, Cell Signaling). Blots were developed using Advanced Molecular Image Imager and
584 ChemoStar Software. Quantification of blots was achieved using ImageJ software v1.44p[61].
585
586 ***Cell fate assays.*** Cell viability and cytotoxicity measurements were performed using
587 CellTiterGlo and CellTox Green assays (both from Promega) according to the manufacturer's
588 instructions. For differentiation, cells were observed using light microscopy and images were
589 taken at 10x, 20x, 40x magnification using an Olympus 2-620 camera connected to Olympus
590 CKX41 microscope. Neurite elongation was measured using the NeuronJ plugin from ImageJ

591 software[61]. Cells with neurite length/cell body width ratios $\geq$2 were considered
592 differentiated. Neurite length was calculated by dividing mean neurite length/differentiated
593 cell; and % differentiation was calculated by dividing the mean % of differentiating cells/total
594 cells in each field of view.
595 For the soft agar assay, 1 ml of 0.8% base agarose layer was placed in each well of 6-
596 well plates, then plates were cooled for 5 min at 4°C to solidify agarose. Then 1 ml of upper
597 agarose layer (0.48%) with 10000 cells was added on the solidified base layer. Then plates
598 were cooled for 5 min, then 1 ml of growth media (+/- 1 µM DPI) was added to each well.
599 Plates were incubated at 37°C and 5% CO_2 for 20 days, monitoring for colony formation. Media
600 (+/- DPI) was replaced every 4 days. Colonies were stained by adding PBS containing 4%
601 formaldehyde and 0.005% crystal violet to each well for 1 hour.
602
603 ***Proteomics and phosphoproteomics.*** Cells were seeded in 15cm^2 dishes in 20 ml culture
604 media. Upon reaching 70-80% confluence, Be(2)-C were treated with 10 µM DPI for 0, 1 and
605 24 hours in reverse order, in triplicates. IMR-5/75 cells were seeded under the same
606 conditions. MYCN expression was downregulated by treating the cells with 1 µg/mL
607 doxycycline. Following MYCN downregulation, cells were treated with 0.5 µM DPI for 24
608 hours, in triplicates. Cells were lysed in ice cold 8M urea/50 mM Tris-HCL pH 8.0,
609 supplemented with phosphatase and protease inhibitors (Roche). Samples were then
610 sonicated for 2 X 9 seconds at 10% power using Branson Sonifier® 250 connected to Syclon
611 Ultrasonic Homogenizer. To reduce protein samples, 8 mM dithithreitol (dTT) was added to
612 the samples and incubated in a thermomixer for 60 minutes at 30°C. Then, samples were
613 alkylated by adding 20 mM iodoacetamide and incubated in a thermomixer for 30 minutes at
614 30°C in the dark. Samples were diluted in 50mM ammonia bicarbonate. 10 µL of sequencing
615 grade trypsin were added into samples and left overnight on a thermomixer at 37°C to allow
616 sample digestion. The following day, formic acid was added to 1% final concentration to stop
617 sample digestion.
618 The Glygen TopTipTM C18 protocol (200µL) was utilized for sample clean up. Samples
619 were centrifuged at 5000 rpm for 5 minutes to remove particulates. 200 µL samples were
620 added into a 1.5mL tube and centrifuged at 3000 rpm for 2 minutes. 200 µL equilibration and
621 washing buffer (0.1% Trifluoracetic acid (TFA) in high performance liquid chromatography
622 (HPLC) grade water were added and the mixtures were centrifuged at 2500 rpm for 2 minutes.
623 Supernatants were dispensed to waste. 200 µL wetting and elution buffer (80% Acetronitrile
624 (ACN) in 0.1% TFA) were added to the pellets and centrifuged at 3000 rpm for 2 minutes.
625 Samples were evaporated for approximately 30 minutes at 30°C in an Eppendorf Concentrator.
626 *TiO_2 (titanium dioxide) phosphopeptide enrichment.* Dried peptide samples were re-
627 suspended in 500 µL Binding Buffer. TiO_2 ratio of beads to sample was weighed out at 10:1. 1
628 mg of TiO_2 was re-suspended in 5 µL of Binding Buffer and mixed on a shaker for 5 minutes at
629 room temperature. 5 µL of TiO_2/Binding Buffer was added to each sample. Supernatants were
630 removed and kept in -80°C. TiO_2 beads were washed with 1 mL Wash Buffer A (80%
631 Acetonitrile, 1% TFA) and centrifuged at 5000 rpm for 1 minute. Wash Buffer A was then

632 removed, and this step was repeated thrice. Next, TiO_2 beads were washed with 1mL Wash
633 Buffer B (80% Acetonitrile, 0.1% TFA) then centrifuged at 5000 rpm for 1 minute. Wash Buffer
634 B was then removed. 50 µL of Elution Buffer (50% Acetonitrile, 25% NH4OH) were added 2
635 times to elute the phosphopeptides. Samples were dried for approximately 20 minutes in an
636 Eppendorf Concentrator at 30°C.
637 *LC-MS/MS Method (Bruker timsTof Pro).* After trypsin digestion and sample clean up
638 using C18 TT2 TopTips (Glygen), samples were run on a Bruker timsTof Pro mass spectrometer
639 connected to a Bruker nanoElute nano-lc chromatography system. Tryptic peptides were
640 resuspended in 0.1% formic acid. Each sample was loaded onto an Aurora UHPLC column
641 (25cm x 75µm ID, C18, 1.6 µm) (Ionopticks) and separated with an increasing acetonitrile
642 gradient over 90 minutes at a flow rate of 250 nl/min at 45°C.
643 The mass spectrometer was operated in positive ion mode with a capillary voltage of
644 1500 V, dry gas flow of 3 l/min and a dry temperature of 180 °C. All data was acquired with
645 the instrument operating in trapped ion mobility spectrometry (TIMS) mode. Trapped ions
646 were selected for ms/ms using parallel accumulation serial fragmentation (PASEF). A scan
647 range of (100-1700 m/z) was performed at a rate of 10 PASEF MS/MS frames to 1 MS scan
648 with a cycle time of 1.16s.
649 *Data analysis.* The raw data was searched against the Homo sapiens subset of the
650 Uniprot Swissprot database (reviewed) using the search engine Fragpipe using specific
651 parameters for trapped ion mobility spectra data dependent acquisition (TIMS DDA). Each
652 peptide used for protein identification met specific Fragpipe parameters, i.e., only peptide
653 scores that corresponded to a false discovery rate (FDR) of 0.01 were accepted from the
654 Fragpipe database search. The normalised protein intensity of each identified protein was
655 used for label free quantitation (LFQ).
656 Data pre-processing and statistical analysis was performed using Perseus (version
657 2.1.2.0)[63] for Figs. 1, 3 and S2 and S3. Phosphoproteomics results were normalized to total
658 proteomics to account for protein abundance. Significant proteins were displayed in a
659 heatmap (FDR < 0.01 for whole proteomics and FDR < 0.05 for phosphoproteomics). Selected
660 proteins were further analysed using DAVID for pathway enrichment[64].
661
662 ***Bioinformatic analysis.*** The Fragpipe proteinGroups.txt files for both the whole- and phospho-
663 proteomics were filtered to remove known contaminants and protein groups containing no
664 protein. LFQ intensity values were log base 2 transformed, with zero values being assigned
665 NaN to circumvent undefined values. Filtering was applied to keep only those
666 proteins/phosphopeptides with at least 6/9 valid values in at least one drug treatment
667 condition. NaN values were then reassigned to zero before median centering. Site- and
668 condition-specific imputation was performed using the scImpute function in PhosR[65] if the
669 protein was quantified in more than 50% of samples from the same drug treatment. Sample-
670 wise tail-based imputation was implemented with the tImpute function[65]. Linear regression
671 models were used to determine the relationship between a protein's expression and its
672 phosphorylation levels. The residuals from the linear models were used to normalize the

673 phosphoproteomics data by the whole proteomics data. Differentially abundant phosphosites
674 and proteins between control and DPI-treated samples were identified using the Limma R
675 package. An FDR threshold of 0.05 was used to determine statistical significance.
676
677 ***Multiset correlation and factor analysis.*** Kinase-substrate relationships were obtained from
678 the PhosphoSitePlus database (https://www.phosphosite.org/homeAction.action), while
679 pathway-gene relationships from the KEGG database were accessed through MSigDB. Both
680 the pathways and kinases were scored in the whole proteomics and phosphoproteomics
681 datasets using the GSVA function in R. The resulting scores, which represent the activity levels
682 of kinases and pathways in each sample, were then used as input for Multiset Correlation and
683 Factor Analysis[26]. This analysis was conducted using default parameters to identify shared
684 factors of variation across both omics' datasets. Kinases and pathways that contributed most
685 to the variation between sample conditions were selected based on their absolute feature
686 loadings.
687
688 ***ChIP-seq data analysis of MYCN binding sites***. ChIP-seq data from the MYCN-amplified
689 neuroblastoma cell line IMR-32 (GEO accession GSE183641) were analyzed using the R2 ChIP-
690 seq Genome Browser (http://r2.amc.nl), focusing on MYCN occupancy at promoter regions.
691 Signal intensity profiles were compared between siControl (IMR32_27_siCtrl MYCN), input
692 (IMR32_25_siCtrl Input) and siMYCN (IMR32_15_siMYCN)-treated conditions to identify
693 differential binding.
694
695 ***Cell fractionation.*** Mitochondria were isolated using the Qproteome Mitochondria Isolation
696 Kit according to manufacturer's instructions (Qiagen). Ten million cells have been used for the
697 isolation of mitochondria and the purity of the fraction was assayed by Western blotting for
698 cytosol (GADPH) or mitochondria (cytochrome C) specific proteins.
699
700 ***MitoSOX Red staining.*** Mitochondrial superoxide levels were assessed using the MitoSOX Red
701 fluorescent indicator (Thermo Scientific) by flow cytometry and live cell imaging, according to
702 manufacturer's instructions.
703 Flow cytometry: $1x10^5$ cells were seeded in a 12 well plate and treated with vehicle
704 (DMSO) or DPI for 24h. After treatment, 1 ml of HBSS buffer with 2.5 µM of MitoSOX™ reagent
705 was added to the cells and incubated for 10 minutes at 37°C. Cells were detached using
706 Versene solution and after two washes in HBBS were re-suspended in 500 ml of HBBS for flow
707 cytometry analysis. Forward and side scatter gates were established to exclude non-viable
708 cells and cell debris from the analysis. Auto-fluorescence signals generated by unlabeled cells
709 were used as negative controls in each experiment. Flow cytometric analysis was performed
710 on an Accuri C6 instrument by using the FL2 detector (Optical Filter 585/40 nm) and analyzed
711 with CFlow® Software (Accuri, Ann Arbor, MI, USA). The data were expressed as median
712 fluorescence intensity of three independent experiments.
713 For imaging, cells were typically seeded in 100 µL of RPMI phenol red-free media per

714 well in duplicate on a black 96-well plate with a clear bottom (Thermo Scientific). To ensure
715 IMR-5/75 and SH-SY5Y/MYCN cells remained attached, the plates were pre-coated with 100
716 µg/mL Poly-D-Lysine (Sigma-Aldrich). 24 hours post-doxycycline induction, the cells were
717 treated with 100 µL of DPI or vehicle and incubated at 37°C. Following the designated
718 incubation period, cells were rinsed once with DPBS containing Ca^{2+}/Mg^{2+} (Invitrogen).
719 MitoSOX Red dye (4 µM) was then added along with the Hoechst 33342 nuclear counterstain
720 (1 µg/mL) (Thermo Scientific) in DPBS containing Ca 2+ /Mg 2+ and incubated for 20 minutes
721 at 37°C, shielded from light. After incubation, cells were washed twice, and fresh RPMI phenol
722 red-free media was added before live-cell imaging. The MitoSOX Red indicator was detected
723 using the Texas Red filter (Ex/Em: 510/580 nm), while Hoechst was detected using the
724 HOECHST 33342 filter (Ex/Em: 353/483 nm).
725
726 ***Live cell imaging.*** Confocal images were captured across four optical planes spaced 1 µm apart
727 (ranging from -1.0 µm to 2.0 µm) within 25 x 25 fields of view, with a 10% overlap per well,
728 using an Opera Phenix High Content Screening System (PerkinElmer). The imaging was
729 performed with either a 40x or 63x/1.15 NA water-immersion objective under live cell
730 conditions (37 °C and 5% CO2). The images obtained were analyzed using an optimized
731 pipeline tailored for each cell line on Harmony® v.4.9 high-content analysis software
732 (PerkinElmer). The software's building blocks were employed to identify and calculate the
733 mean dye parameters per well, including the number of nuclei and MitoSOX Red mean
734 intensity per cell.
735
736 ***RT-qPCR.*** Total RNA was isolated from NB cell lysates using the RNeasy kit (Qiagen, UK).
737 Reverse transcription was carried out on 1000 ng of total RNA using Superscipt III reverse
738 transcriptase (Invitrogene) according to the manufacturers' instructions. Quantification of
739 gene expression by real-time PCR was performed on an ABI Prism 7700 Sequence Detection
740 System, (Applied Biosystems Inc., UK). MT-ND1, MT-ND2, MT-ND3, MT-ND4L, MT-ND6, MT-
741 ATP6, MT-ATP8, MT-CO1, MT-CYB, TFAM, and MYCN gene expression was examined using
742 specific Taqman gene expression assays (Applied Biosystems Inc., UK). GADPH was used as
743 endogenous control in the assay.
744
745 ***Metabolic measurements.*** Metabolic activity was evaluated using a Seahorse XF24 Analyzer
746 (Seahorse Biosciences) through an ATP rate test. IMR-5/75 and SH-SY5Y/MYCN cells were
747 seeded at 37,500 cells per well in PDL-coated XF microplates and incubated in XF RPMI
748 medium with glucose, sodium pyruvate, and glutamine. After six hours, doxycycline was
749 added to induce gene expression in specific wells. On the second day, cells were treated with
750 DPI or vehicle, and the XFe24 Sensor Cartridge was hydrated overnight. On the third day, cells
751 were washed with assay medium, incubated, and the ATP rate test was conducted by
752 sequentially injecting oligomycin A and a mix of rotenone and antimycin A. Post-assay, cells
753 were fixed with glutaraldehyde, stained with Crystal Violet for normalization, and absorbance
754 was measured. Data was analyzed using Wave software to generate key metabolic

755 parameters, including Oxygen Consumption Rate (OCR), Proton Efflux Rate (PER), and
756 Extracellular Acidification Rate (ECAR), followed by statistical analysis in GraphPad Prism.
757
758 ***Zebrafish experiments*** were approved by the University College Dublin Animal Research
759 Ethics Committee and the Healthcare Products Regulatory Authority (AE18982/P038).
760 zebrafish (Danio rerio) were maintained at 28°C on a 14-hour light/10-hour dark cycle.
761 Xenografts: At 2dpf, dechorionated zebrafish embryos were microinjected with fluorescently
762 labelled Be(2)-C cells. Prior to microinjection, embryos were transferred to prewarmed 2%
763 agarose gel and anaesthetized with 0.05mg/mL Tricaine. Be(2)-C cells were fluorescently
764 labelled with DiI. Approximately 100-500 cells were injected into the perivitelline space of
765 each embryo. Following injection, embryos were screened and randomly assigned a
766 treatment arm. Each embryo was placed in an individual well of 24 well plate containing 600uL
767 PTU ± DPI (1 uM). Embryos were incubated at 35 °C for duration of treatment (72 h). Embryos
768 were imaged daily using fluorescent microscopy (Nikon Eclipse C1) to monitor tumour
769 progression and metastasis. Data analysis was carried out using ImageJ, Excel and GraphPad
770 Prism.
771 The Tg[dbh:MYCN-EGFP] transgenic zebrafish was a generous gift from A. T. Look (Dana-Farber
772 Cancer Institute, Harvard Medical School)[51]. Adult Tg[dbh:MYCN-EGFP] zebrafish were
773 monitored for fluorescent tumor masses biweekly. Zebrafish developing the fish-equivalent of
774 human neuroblastoma in the interrenal gland (age, 15 months; n = 4) were treated every 48
775 hours with DPI for 2 weeks. Variance in tumor size for all fish at pretreatment was <5%.
776 Zebrafish were anesthetized by 0.016% tricaine before microscopic analysis. An Olympus
777 SZX10 fluorescence stereomicroscope equipped with an Olympus DP71 camera was used to
778 capture images. The fluorescent region posterior to the gills, which corresponds to the region
779 of neuroblastoma growth[51], was analyzed using ImageJ software (version 1.44p).
780

781 **Acknowledgements**
782 This work received funding from Science Foundation Ireland and National Children's Research
783 Centre / Children's Health Ireland through the Precision Oncology Ireland grant 18/SPP/3522,
784 the Research Ireland Frontiers for the Future Program grant 22/FFP-A/10729, the Irish
785 Research Council grant GOIPG/2020/1361, the Pathological Society of Great Britain and
786 Ireland, Horizon 2020 programme grant H2020-RISE/GA734907 (3D-NEONET), European
787 Union FP7 grant 259348-2 "ASSET," and financial support of Children's Health Foundation
788 under the management of Science Foundation Ireland under the Frontiers for the Future
789 Programme Grant Number 21/FFP-P/10130. Mass spectrometry was performed at The
790 Comprehensive Molecular Analytical Platform which was funded by The Research Ireland
791 Research Infrastructure Programme (18/RI/5702). This project was partially supported by the
792 Fight Kids Cancer Funding Programme, supported by Imagine for Margo, KickCancer,
793 Fondatioun Kriibskrank Kanner, Federazione Italiana Associazioni Genitori e Guariti
794 Oncoematologia Pediatrica (FIAGOP), and Cris Cancer Foundation.

Author contributions

Conceptualization, W.K. and M.H.; Investigation, S.E., St.M., A.A., Si.M., K.I., K.W., M.H.; Formal Analysis, S.E., St.M., K.I., M.H., D.E.; Writing - all authors contributed to writing the manuscript; Visualization, S.E., D.E., M.H.; Funding Acquisition, W.K., M.H., L.J., St.M., A.A.; Resources, K.I., K.W., L.J.; Supervision, L.J., M.H., and W.K.

Declaration of interests

L.J. is shareholder in BioReperia AB, a company that is developing zebrafish xenograft models for diagnosis and prognosis of cancer patients. The other authors declare no conflicts of interest.

References

1. Matthay, K.K., et al., *Neuroblastoma.* (2056-676X (Electronic)).
2. Friedman, D.N. and T.O. Henderson, *Late Effects and Survivorship Issues in Patients with Neuroblastoma.* Children (Basel), 2018. **5**(8).
3. Otte, J., et al., *MYCN Function in Neuroblastoma Development.* Front Oncol, 2020. **10**: p. 624079.
4. Wolpaw, A.J., et al., *Drugging the "Undruggable" MYCN Oncogenic Transcription Factor: Overcoming Previous Obstacles to Impact Childhood Cancers.* Cancer Res, 2021. **81**(7): p. 1627-1632.
5. Epp, S., S.M. Chuah, and M. Halasz, *Epigenetic Dysregulation in MYCN-Amplified Neuroblastoma.* Int J Mol Sci, 2023. **24**(23).
6. Ruiz-Pérez, M.V., A.B. Henley, and M. Arsenian-Henriksson, *The MYCN Protein in Health and Disease.* Genes (Basel), 2017. **8**(4).
7. Riganti, C., et al., *Diphenyleneiodonium inhibits the cell redox metabolism and induces oxidative stress.* J Biol Chem, 2004. **279**(46): p. 47726-31.
8. Lambert, A.J., et al., *Diphenyleneiodonium acutely inhibits reactive oxygen species production by mitochondrial complex I during reverse, but not forward electron transport.* Biochim Biophys Acta, 2008. **1777**(5): p. 397-403.
9. Alborzinia, H., et al., *MYCN mediates cysteine addiction and sensitizes neuroblastoma to ferroptosis.* Nat Cancer, 2022. **3**(4): p. 471-485.
10. Wang, T., et al., *MYCN drives glutaminolysis in neuroblastoma and confers sensitivity to an ROS augmenting agent.* Cell Death Dis, 2018. **9**(2): p. 220.
11. Brady, S.W., et al., *Pan-neuroblastoma analysis reveals age- and signature-associated driver alterations.* Nat Commun, 2020. **11**(1): p. 5183.

12. Duffy, D.J., et al., *Integrative omics reveals MYCN as a global suppressor of cellular signalling and enables network-based therapeutic target discovery in neuroblastoma.* Oncotarget, 2015. **6**(41): p. 43182-201.

13. Svensson, A., et al., *Digoxin inhibits neuroblastoma tumor growth in mice.* Anticancer Res, 2005. **25**(1a): p. 207-12.

14. Russo, V.C., et al., *Antiapoptotic effects of leptin in human neuroblastoma cells.* Endocrinology, 2004. **145**(9): p. 4103-12.

15. Dzieran, J., et al., *MYCN-amplified neuroblastoma maintains an aggressive and undifferentiated phenotype by deregulation of estrogen and NGF signaling.* Proc Natl Acad Sci U S A, 2018. **115**(6): p. E1229-e1238.

16. Bierbrauer, A., et al., *A direct comparison of selective BH3-mimetics reveals BCL-X(L), BCL-2 and MCL-1 as promising therapeutic targets in neuroblastoma.* Br J Cancer, 2020. **122**(10): p. 1544-1551.

17. Lamers, F., et al., *Targeted BCL2 inhibition effectively inhibits neuroblastoma tumour growth.* Eur J Cancer, 2012. **48**(16): p. 3093-103.

18. Phimmachanh, M., et al., *Histone Deacetylases and Histone Deacetylase Inhibitors in Neuroblastoma.* Front Cell Dev Biol, 2020. **8**: p. 578770.

19. Krstic, A., et al., *A Chemo-Genomic Approach Identifies Diverse Epigenetic Therapeutic Vulnerabilities in MYCN-Amplified Neuroblastoma.* Front Cell Dev Biol, 2021. **9**: p. 612518.

20. Hastings, J.F., et al., *Memory of stochastic single-cell apoptotic signaling promotes chemoresistance in neuroblastoma.* Sci Adv, 2023. **9**(9): p. eabp8314.

21. Messina, E., et al., *Guanine nucleotide depletion triggers cell cycle arrest and apoptosis in human neuroblastoma cell lines.* Int J Cancer, 2004. **108**(6): p. 812-7.

22. Moreno, L., et al., *A phase I trial of AT9283 (a selective inhibitor of aurora kinases) in children and adolescents with solid tumors: a Cancer Research UK study.* Clin Cancer Res, 2015. **21**(2): p. 267-73.

23. Fetahu, I.S. and S. Taschner-Mandl, *Neuroblastoma and the epigenome.* Cancer and Metastasis Reviews, 2021. **40**(1): p. 173-189.

24. Li, X. and L.H. Jiang, *A critical role of the transient receptor potential melastatin 2 channel in a positive feedback mechanism for reactive oxygen species-induced delayed cell death.* J Cell Physiol, 2019. **234**(4): p. 3647-3660.

25. Yamamuro-Tanabe, A., et al., *Proteasome inhibitors induce apoptosis by superoxide anion generation via NADPH oxidase 5 in human neuroblastoma SH-SY5Y cells.* J Pharmacol Sci, 2024. **155**(2): p. 52-62.

26. Brown, B.C., et al., *Multiset correlation and factor analysis enables exploration of multi-omics data.* Cell Genomics, 2023. **3**(8): p. 100359.

866 27. Nguyen, T.T.T., et al., *Aurora kinase A inhibition reverses the Warburg effect and elicits*
867 *unique metabolic vulnerabilities in glioblastoma.* Nat Commun, 2021. **12**(1): p. 5203.

868 28. Prickaerts, P., et al., *MK3 modulation affects BMI1-dependent and independent cell cycle*
869 *check-points.* PLoS One, 2015. **10**(4): p. e0118840.

870 29. Rosario, S.R., et al., *Pan-cancer analysis of transcriptional metabolic dysregulation using*
871 *The Cancer Genome Atlas.* Nat Commun, 2018. **9**(1): p. 5330.

872 30. Belosludtseva, N.V., L.A. Matveeva, and K.N. Belosludtsev, *Mitochondrial Dyshomeostasis*
873 *as an Early Hallmark and a Therapeutic Target in Amyotrophic Lateral Sclerosis.* Int J Mol
874 Sci, 2023. **24**(23).

875 31. Kim, J.E., et al., *LIM kinase-2 induces programmed necrotic neuronal death via dysfunction*
876 *of DRP1-mediated mitochondrial fission.* Cell Death Differ, 2014. **21**(7): p. 1036-49.

877 32. Xie, B., et al., *Cyclin B1/CDK1-regulated mitochondrial bioenergetics in cell cycle*
878 *progression and tumor resistance.* Cancer Lett, 2019. **443**: p. 56-66.

879 33. Ahn, M., et al., *A requirement for PAK1 to support mitochondrial function and maintain*
880 *cellular redox balance via electron transport chain proteins to prevent β-cell apoptosis.*
881 Metabolism, 2021. **115**: p. 154431.

882 34. Yeh, E., et al., *A signalling pathway controlling c-Myc degradation that impacts oncogenic*
883 *transformation of human cells.* Nat Cell Biol, 2004. **6**(4): p. 308-18.

884 35. Nolfi-Donegan, D., A. Braganza, and S. Shiva, *Mitochondrial electron transport chain:*
885 *Oxidative phosphorylation, oxidant production, and methods of measurement.* Redox Biol,
886 2020. **37**: p. 101674.

887 36. Doroshow, J.H., R.S. Esworthy, and F.F. Chu, *Control of doxorubicin-induced, reactive*
888 *oxygen-related apoptosis by glutathione peroxidase 1 in cardiac fibroblasts.* Biochem
889 Biophys Rep, 2020. **21**: p. 100709.

890 37. Muth, D., et al., *Transcriptional repression of SKP2 is impaired in MYCN-amplified*
891 *neuroblastoma.* Cancer Res, 2010. **70**(9): p. 3791-802.

892 38. Redza-Dutordoir, M. and D.A. Averill-Bates, *Activation of apoptosis signalling pathways by*
893 *reactive oxygen species.* Biochim Biophys Acta, 2016. **1863**(12): p. 2977-2992.

894 39. Garrido, C., et al., *Mechanisms of cytochrome c release from mitochondria.* Cell Death
895 Differ, 2006. **13**(9): p. 1423-33.

896 40. Morrish, F., C. Giedt, and D. Hockenbery, *c-MYC apoptotic function is mediated by NRF-1*
897 *target genes.* Genes Dev, 2003. **17**(2): p. 240-55.

898 41. Hanahan, D., *Hallmarks of Cancer: New Dimensions.* Cancer Discov, 2022. **12**(1): p. 31-46.

899 42. Kang, J.H., et al., *MYCN silencing induces differentiation and apoptosis in human*
900 *neuroblastoma cells.* Biochem Biophys Res Commun, 2006. **351**(1): p. 192-7.

901 43. Franken, N.A., et al., *Clonogenic assay of cells in vitro.* Nat Protoc, 2006. **1**(5): p. 2315-9.

902 44. Matthay, K.K., et al., *Treatment of high-risk neuroblastoma with intensive chemotherapy,*
903 *radiotherapy, autologous bone marrow transplantation, and 13-cis-retinoic acid.*
904 *Children's Cancer Group.* N Engl J Med, 1999. **341**(16): p. 1165-73.

905 45. Veschi, V., F. Verona, and C.J. Thiele, *Cancer Stem Cells and Neuroblastoma: Characteristics*
906 *and Therapeutic Targeting Options.* Front Endocrinol (Lausanne), 2019. **10**: p. 782.

907 46. Mahller, Y.Y., et al., *Neuroblastoma cell lines contain pluripotent tumor initiating cells that*
908 *are susceptible to a targeted oncolytic virus.* PLoS One, 2009. **4**(1): p. e4235.

909 47. Qin, X., et al., *CKLF instigates a "cold" microenvironment to promote MYCN-mediated*
910 *tumor aggressiveness.* Sci Adv, 2024. **10**(11): p. eadh9547.

911 48. Anderson, N.M., et al., *Metabolic Enzyme DLST Promotes Tumor Aggression and Reveals a*
912 *Vulnerability to OXPHOS Inhibition in High-Risk Neuroblastoma.* Cancer Res, 2021. **81**(17):
913 p. 4417-4430.

914 49. Zhu, S., et al., *LMO1 Synergizes with MYCN to Promote Neuroblastoma Initiation and*
915 *Metastasis.* Cancer Cell, 2017. **32**(3): p. 310-323.e5.

916 50. Tao, T., et al., *The pre-rRNA processing factor DEF is rate limiting for the pathogenesis of*
917 *MYCN-driven neuroblastoma.* Oncogene, 2017. **36**(27): p. 3852-3867.

918 51. Zhu, S., et al., *Activated ALK collaborates with MYCN in neuroblastoma pathogenesis.*
919 Cancer Cell, 2012. **21**(3): p. 362-73.

920 52. Aldieri, E., et al., *Classical inhibitors of NOX NAD(P)H oxidases are not specific.* Curr Drug
921 Metab, 2008. **9**(8): p. 686-96.

922 53. Gustafson, W.C., et al., *Drugging MYCN through an allosteric transition in Aurora kinase A.*
923 Cancer Cell, 2014. **26**(3): p. 414-427.

924 54. Mossé, Y.P., et al., *A Phase II Study of Alisertib in Children with Recurrent/Refractory Solid*
925 *Tumors or Leukemia: Children's Oncology Group Phase I and Pilot Consortium (ADVL0921).*
926 Clin Cancer Res, 2019. **25**(11): p. 3229-3238.

927 55. Roeschert, I., et al., *Combined inhibition of Aurora-A and ATR kinase results in regression*
928 *of MYCN-amplified neuroblastoma.* Nat Cancer, 2021. **2**(3): p. 312-326.

929 56. Liu, Z., et al., *Targeting MYCN in Pediatric and Adult Cancers.* Front Oncol, 2020. **10**: p.
930 623679.

931 57. Wasylishen, A.R., et al., *MYC phosphorylation at novel regulatory regions suppresses*
932 *transforming activity.* Cancer Res, 2013. **73**(21): p. 6504-15.

933 58. Oliynyk, G., et al., *MYCN-enhanced Oxidative and Glycolytic Metabolism Reveals*
934 *Vulnerabilities for Targeting Neuroblastoma.* iScience, 2019. **21**: p. 188-204.

59. Mukherjee, S., et al., *Targeting mitochondria as a potential therapeutic strategy against chemoresistance in cancer.* Biomed Pharmacother, 2023. **160**: p. 114398.

60. Epp, S., et al., *OXPHOS TARGETING OF MYCN-AMPLIFIED NEUROBLASTOMA.* bioRxiv, 2024: p. 2024.08.03.606365.

61. Schneider, C.A., W.S. Rasband, and K.W. Eliceiri, *NIH Image to ImageJ: 25 years of image analysis.* Nature Methods, 2012. **9**(7): p. 671-675.

62. Halasz, M., et al., *Integrating network reconstruction with mechanistic modeling to predict cancer therapies.* Science Signaling, 2016. **9**(455): p. ra114-ra114.

63. Tyanova, S., et al., *The Perseus computational platform for comprehensive analysis of (prote)omics data.* Nature Methods, 2016. **13**(9): p. 731-740.

64. Sherman, B.T., et al., *DAVID: a web server for functional enrichment analysis and functional annotation of gene lists (2021 update).* Nucleic Acids Research, 2022. **50**(W1): p. W216-W221.

65. Kim, H.J., et al., *PhosR enables processing and functional analysis of phosphoproteomic data.* Cell Reports, 2021. **34**(8): p. 108771.